



# Laser-pump/X-ray-probe experiments with electrons ejected from a Cu(111) target: space-charge acceleration

G. Schiwietz,\* D. Kühn, A. Föhlich, K. Holldack, T. Kachel and N. Pontius

Received 22 February 2016

Accepted 6 June 2016

Edited by S. M. Heald, Argonne National Laboratory, USA

**Keywords:** picosecond-pump-probe experiments; time-resolved XPS; time-resolved NEXAFS; photoelectrons; Auger electrons.

Institut Methoden und Instrumentierung der Forschung mit Synchrotronstrahlung (FG-ISRR), Helmholtz-Zentrum Berlin für Materialien und Energie GmbH, Hahn-Meitner-Platz 1, 14109 Berlin, Germany.

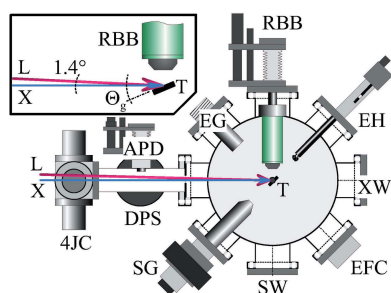
\*Correspondence e-mail: schiwietz@helmholtz-berlin.de

A comprehensive investigation of the emission characteristics for electrons induced by X-rays of a few hundred eV at grazing-incidence angles on an atomically clean Cu(111) sample during laser excitation is presented. Electron energy spectra due to intense infrared laser irradiation are investigated at the BESSY II slicing facility. Furthermore, the influence of the corresponding high degree of target excitation (high peak current of photoemission) on the properties of Auger and photoelectrons liberated by a probe X-ray beam is investigated in time-resolved pump and probe measurements. Strong electron energy shifts have been found and assigned to space-charge acceleration. The variation of the shift with laser power and electron energy is investigated and discussed on the basis of experimental as well as new theoretical results.

## 1. Introduction

Electron spectroscopy provides many tools for the investigation of atoms, molecules, clusters and solids. Excitation by electrons, ions or photons enables gaining not only information on the surface composition (NIST, 2005; see also Smekal *et al.*, 2005) but also detailed insights into electronic structure and even electron dynamics, especially if time-resolved measurements are used. In the photon-energy range studied here, about 300–1000 eV, X-ray-induced inelastic processes are clearly dominated by (dipolar) photo-ionization. The rates of other possible mechanisms (such as direct energy transfer to the nuclei or Compton scattering) are lower by several orders of magnitude. The first local response of a lattice atom to an X-ray ionization event is an extremely rapid inner-shell relaxation within a few attoseconds ( $10^{-18}$  s), followed by a build-up of a conduction-band screening cloud on a sub-femtosecond time scale for typical metals (Borisov *et al.*, 2004).

The electron dynamics of the resulting dressed electrons (faster electrons with attached screening cloud) depends on the geometry of the irradiated volume, on the excitation densities and on the target energy-dissipation channels. For *fast incident ions* or other swift charged particles, there is a long columnar electronic excitation profile with a sub-nanometer diameter and many micrometers in depth (Schiwietz *et al.*, 2004). For *visible and near-visible laser irradiation*, there is a flat electronic excitation profile with a depth of a few nanometers and typically at least several micrometers in diameter. A focused keV-X-ray beam involves a variable excitation volume with diameters of many micrometers and absorption depths extending from the nanometer to the micrometer scale, dependent on the material and photon



© 2016 International Union of Crystallography

energy. In the following we will concentrate on a situation where a relatively weak X-ray probe beam is focused onto the center of an intense infrared (IR) laser pump-beam on a metallic target (experiments have been performed with Cu samples and specifications of the irradiation and detection geometries will be given in the next section).

Dressed electron–electron collisions give rise to a local thermalization of the non-equilibrium energy distribution after the excitation or ionization event (Fann *et al.*, 1992; Schiwietz *et al.*, 2000). For Cu targets at low excitation densities there is plenty of information and relaxation times have been measured (in some cases even inelastic lifetimes may be separated) as a function of intermediate-state energy levels (Schmittenmaer *et al.*, 1994; Cao *et al.*, 1997; Knoesel *et al.*, 1998; Lisowski *et al.*, 2004). These relaxation times increase from 4 to 450 fs when the excitation energies are lowered from 3.2 eV to 0.1 eV. A Cu-crystal-surface dependence of the relaxation (Ogawa *et al.*, 1997) and de-coherence of Cu-*d*-band holes (Petek *et al.*, 1999) have been found as well. Theoretically, the corresponding inelastic lifetimes of hot electrons seem to be understood quite well (Campillo *et al.*, 1999). At high electron temperatures (high laser-excitation power density) additional excitation channels open up (Arista & Brandt, 1984), but enhanced electron screening leads to an all-over reduction of inelastic transition rates and a corresponding enhancement of self-consistent inelastic lifetimes in a free electron gas (Echenique, 2007). For fast electrons in materials with an electronic gap or also at high electron temperature, this may be different (Schiwietz *et al.*, 2007).

Hot electrons do not only collide with each other but they also diffuse through the materials driven by temperature gradients (Martynenko & Yavlinkii, 1983). Furthermore, especially after short-pulsed initial excitation processes, ballistic electron transport may provide an important cooling mechanism (Brorson *et al.*, 1987). This spatial redistribution of momenta and electron energies takes 10 to 100 fs for an excitation depth of 10 nm below the surface [similar values have been found for primary ions as well (Schiwietz *et al.*, 2004, 2008)]. A certain fraction of the hot electrons overcome the surface-potential barrier. The resulting surface charging as well as direct electronic interactions may strongly influence the dynamics of ejected electrons and bound electrons close to the surface (such effects will be discussed later on in more detail). Specifically space-charge-driven electron–electron interactions are very important for understanding and improving electron-spectroscopy methods related to state-of-the-art X-ray and UV excitations sources (Gregoratti *et al.*, 2009; Schönhense *et al.*, 2015). The theoretical understanding of these short-time effects has made large progress in recent times (Lemell *et al.*, 2003; Bagesen & Madsen, 2008).

Thermal equilibrium with the lattice is the final stage of the non-equilibrium dynamics and two main mechanisms are expected to be responsible for the energy transfer from the hot electron system to the atoms. One mechanism is the so-called cold melting (Stampfli & Bennemann, 1994; Silvestrelli *et al.*, 1996) or spontaneous lattice-instability, where atomic motion is triggered by modified inter-atomic potentials. The

other mechanism is the well known electron–phonon (Kaganov *et al.*, 1956; Rethfeld *et al.*, 2002; Ferrini *et al.*, 2009) or electron–ion interaction. The coupling time of the electronic degrees of freedom with the atomic motion (*e.g.* lattice vibrations) ranges from 50 fs (*via* cold melting; see Wall *et al.*, 2013; Schiwietz *et al.*, 2010) to hundreds of picoseconds *via* electron–phonon couplings.

In this work, however, we focus on the electron dynamics by measuring the laser-induced ejected hot electrons directly and by investigating the effect of laser excitation on the Cu-*L* absorptions structures as well as on the energy distribution of fast ejected electrons. We show that vacuum space-charge effects may have an enormous influence on the emission of electrons even at high velocities. Before the corresponding results are shown and interpreted, the experimental and theoretical methods shall be presented in the next two sections.

## 2. Experimental methods

All experimental investigations performed in this work are based on electron spectroscopy and target-current measurements for electron-ejection from different Cu samples due to laser and/or X-ray pulses. Our electron-timing (ET) chamber, a mobile ultra-high-vacuum scattering chamber at residual pressures of  $1.2 \times 10^{-10}$  to  $5 \times 10^{-10}$  mbar, has been used for the various experimental runs at the BESSY II storage ring of the Helmholtz-Zentrum Berlin. Preparation measurements have been performed at the PM3 beamline (Kachel, 2016) and the same ET chamber has been installed and operated at the UE56/1\_PGM-1 beamline (Holldack *et al.*, 2014; Pontius *et al.*, 2016) for all experiments involving laser pulses in single-beam as well as pump–probe experiments.

Fig. 1 displays a top view of the whole experimental setup, the ET chamber with the main attached devices. The X-ray

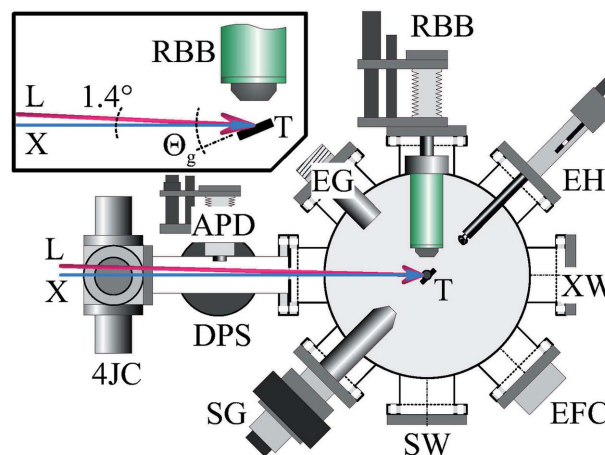


**Figure 1** Experimental setup (horizontal plane): electron-timing (ET) chamber with incident X-ray (blue arrow, marked X) and laser (broader pink arrow, marked L) beams. The electrostatic RBB electron spectrometer (shaded in green) is placed in the horizontal plane at  $90^\circ$  with respect to the X-ray beam. The inset shows the fixed angle between X-ray and laser beams as well as the grazing angle  $\Theta_g$  between the X-ray beam (on the beamline axis) and the target surface. For further explanations see text.

**Table 1**  
Typical parameters for incident photons and escaping electrons used in this work.

	Energy $E_X$ , $E_{IR}$ or $E_e$	Resolution $\Delta E/E$	Attenuation/ escape depth $d$	Spot size $x$ (horizontal)	Spot size $y$ (vertical)
X-ray	315–1000 eV	<0.1%	15–250 nm	270 $\mu\text{m}$	60 $\mu\text{m}$
IR laser	1.55 eV	<0.5%	3–5 nm	1200 $\mu\text{m}$	400 $\mu\text{m}$
Electrons	20–1000 eV	3%	0.5–1.7 nm	–	–

beam (marked X) and laser beam (marked L) are indicated as arrows. Both beams pass through a four-jaw collimator (4JC) and a differential pumping stage (DPS) in front of the main chamber. A windowless avalanche photodiode (APD) enables the timing of the laser pulses to be adjusted relative to the X-ray beam pulses with a time resolution below about 100 ps. The inset shows the angles involved, specifically the grazing angle  $\Theta_g$  between the X-ray beam and the surface of the (movable) sample. The sample-holder system allows for a linear motion in the vertical direction as well as a rotation around this axis, in order to change  $\Theta_g$ . It consists of a sample ladder for three different targets T and an alignment plate at the end of the sample-holder system. A small circular aperture in the alignment plate is centered exactly below the three sample positions and it is used as a metering orifice by measuring the electrical current at the sample-holder system. The electron spectrometer and most other devices are placed in the same horizontal plane and are described in the following.

For the electron analysis, we have used the newly developed retarding Bessel box RBB (Schiwietz *et al.*, 2015) at an angle of 90° with respect to the primary X-ray beam. This RBB spectrometer is a small and robust electrostatic spectrometer, featuring a large detection solid-angle (nearly 2% of the hemisphere) and also well defined timing properties with an integral time resolution of about 2 ns for fast detected electrons. Compared with the published version of the RBB, we have modified the entrance nozzle in order to reduce slit scattering and enable smaller distances between spectrometer and target surface. The RBB was mounted on an  $x/y/z$ -translation stage, and, for electron-pulse detection, it is equipped with a chevron-type double channel-plate (resistivity matched detection-grade type, with an aspect ratio of 60:1, delivered by Tectra, Germany). Direct electron counting or alternatively event-mode data acquisition have been used (saving the measured pulse height as well as the electron time-of-flight). During the first tests, the Cu target was biased to +2 keV, thereby suppressing electron ejection, in order to check for influence of scattered X-ray and laser photons on the spectra.

For preparation purposes and optimization of the setup, measurements have been performed with incident electrons, using primary electron energies between 500 eV and 5 keV as delivered by the internal electron gun (EG) of the scattering chamber. The center of the chamber and of the samples is defined by focusing the various primary beams (electron, X-ray and laser) through the circular aperture on the alignment plate. The internal electron beam may be focused onto the electron Faraday cup (EFC). The laser and X-ray beam

can be visualized on the exit window (XW) with fluorescence coating. The position of the RBB was pre-aligned through the side window (SW) and finally adjusted using keV back-scattered electrons or emitted target electrons.

Single-crystalline Cu(100), Cu(110) and Cu(111) targets (produced by MaTecK, Germany) have been used in the different experiments. Atomically clean surfaces have been prepared by cycles of sputter erosion with an internal Ar sputter-ion gun (SG) and sample annealing up to about 580°C, using electron-beam heating (EH) from the back side of the samples. All experiments have been performed at room temperature, with an estimated maximum increase of the mean target temperature below 20 K at the highest laser powers. X-ray photoelectron ejection of Cu and Cu-LMM Auger-electron emission is well investigated for this case (Courths & Hüfner, 1984). Thus, much published data on various spectroscopies for clean Cu samples does exist. X-ray photoelectron spectroscopy (XPS), absorption spectroscopy and Auger analysis have been used to exclude substantial surface coverages by residual-gas molecules after the sputter/annealing cycles.

Table 1 summarizes typical experimental conditions regarding the two incident beams (IR laser and X-rays) as well as of the detected electrons used during the experiments discussed later on. Data for the projected IR absorption depth [see Polyanskiy (2015), for a wavelength of  $\lambda_{IR} = 800$  nm] and projected X-ray absorption depth (Polyanskiy, 2015; Henke *et al.*, 1993) have been taken from tabulations including many different sources. The given horizontal extensions for the incident beams are corrected by a factor of three, corresponding to grazing-incident angles around  $\Theta_g = 20^\circ$ . The electron escape depth for the different line structures is mainly given by the electron inelastic mean-free path (IMFP). We use recommended IMFP values (NIST, 2000), without an additional correction, because the electron-detection angle is close to normal.

From the table one may extract that the information depth of all experiments is given by the electron IMFP and thus limited to the top two to five surface layers of Cu. The lateral resolution in the pump–probe experiments is determined by the projection of the X-ray beam spot onto the sample surface. Both photon beams are centered in the focal point of the beamline, as was verified by optical inspection with the fluorescence coated alignment plate. The laser beam is significantly broader than the X-ray beam and, thus, it yields a nearly constant power density across the X-ray spot. The small angle between laser and X-ray beam gives rise to a transit-time broadening at the target surface below 25 fs (for the given

horizontal X-ray spot size) and can thus be neglected. The laser arrival-time distribution due to the target tilt may lead to a broadening of up to 3 ps, if long-range interactions are important, *e.g.* in the electron-detection process.

### 3. Theoretical treatment of vacuum space-charge acceleration

In the following, we describe a simple model calculation of the vacuum space-charge acceleration. We use a largely analytical solution for the cylinder-symmetrical case, without the statistical restrictions of the charged-particle transport simulations that have largely been used so far. In this analytical solution, we will not be able to include process details, such as coupling to surface plasmons, full electron exchange and correlation in the continuum, non-linearity in the surface neutralization and in the time-dependence of the image charge. However, except for electron correlation these effects have also been neglected in the previous calculations. Electron correlation in the continuum corresponds to mutual energy transfers *via* the residual electron interactions (collision terms). For the present non-equilibrium case, it results in a stochastic perturbation, the so-called Boersch effect (Boersch, 1954; Jansen, 1988). Its possible influence will be discussed at the end of this section.

The subsequent treatment is based on a more realistic consideration of the low-energy electrons that make up the space charge. In the following, these laser-induced electrons are named *charge cloud* and the individual faster electrons that are generated by the X-ray beam are named *test electrons*. Our mean-field estimate of space-charge acceleration due to an intense charge cloud interacting with such test electrons ejected from a metal surface is based on some simplifying assumptions:

(i) The charge-cloud electrons are either slow enough or their density is low enough (below the material destruction limit) that a simple adiabatic as well as linear electron screening potential with a mirror-charge concept is valid (Zhou *et al.*, 2005; Hellmann *et al.*, 2009; Bergara *et al.*, 1998).

(ii) The slow charge-cloud electrons do mainly follow the typical  $\cos$  angular distribution function (Rösler, 1995) and the transversal motion of the charge-cloud component is considered as a time-dependent growth and motion of the electron and mirror-charge disks, assuming a nearly ballistic motion (defined further below).

(iii) We restrict the treatment to the interaction of a test electron that moves from the center of a slow electron-emission disk (the laser spot is large compared with the X-ray spot) in the axial direction (the direction of the surface normal).

(iv) We neglect the small difference between the electron depths of origin (relative to the image-charge symmetry plane) and between the transport times for the two electron fractions.

We consider only the electric field  $E_z(x = 0, y = 0, z) = E_z(z)$  in the  $z$  direction (surface-normal direction) and directly on the  $z$  axis, the symmetry axis of a uniformly charged flat disk centered in the  $xy$  plane. The integrated electric field components in the  $xy$  plane cancel by symmetry, and the  $z$ -

component of the field may be obtained by linear superposition. The two-dimensional integration of the Coulomb field over the disk with radius  $R$  in the  $xy$  plane finally yields (detailed derivations may be found in text books or on the web)

$$E_z(z, R) = \frac{\text{sign}(z)\sigma}{2\epsilon_0} \left[ 1 - \frac{z}{(z^2 + R^2)^{1/2}} \right] = \frac{\text{sign}(z)c}{R^2} \left[ 1 - \frac{1}{(1 + R^2/z^2)^{1/2}} \right], \quad (1)$$

where  $\sigma$  is the area charge-density (corresponding to the total charge  $Q$ ),  $\epsilon_0$  is the vacuum permittivity and  $c = Q/2\pi\epsilon_0$ . The ‘sign’ function is defined in the typical way,  $\text{sign}(x) = -1$  for negative arguments  $x$  and  $\text{sign}(x) = 1$  otherwise. In a next step, one might replace an extended realistic charge-cloud distribution by a superposition of flat disks. As will be shown further below, however, we may circumvent this extra integration. In the actual calculations, we use the result of equation (1) for the description of a moving charge disk (a subset of the slow electrons with fixed longitudinal velocity) at distance  $d$  from the surface and the corresponding image charges at distance  $-d$  (with area charge-density  $-\sigma$ ). This resulting dynamic electric field  $E_z^{\text{dyn}}(z, d, R)$  at the position  $z$  of a test particle may be written as

$$E_z^{\text{dyn}}(z, d, R) = E_z(z - d, R) - E_z(z + d, R). \quad (2)$$

In the limit  $|z| < d \ll R$  (a position in between the large charged disk and its image charge distribution) we arrive at the  $z$ -independent solution  $E_z^{\text{dyn}}(z, R, d) \simeq (-2c/R^2) = -\sigma/\epsilon_0$ , corresponding to the (reverse) electric field in the center of a capacitor that consists of two oppositely charged and closely spaced electrodes with area charge-densities  $\sigma$  and  $-\sigma$ . For large distances  $z$  (corresponding to large subtraction errors), we use the first term of the Taylor series as a replacement of equations (1) and (2). For large times, the effective radius of the charged disk  $R_{\text{eff}}$  is assumed to increase roughly equal to the distance  $d$ , simulating a  $45^\circ$  emission angle ( $\alpha = \pi/4$ ), consistent with a cosine angular distribution of the space-charge electrons,

$$R_{\text{eff}}(t) \simeq \left[ R_0^2 + \tan^2(\alpha) d^2(t) \right]^{1/2}. \quad (3)$$

At small times  $t$  the disk size is given by the spot radius  $R_0$  of the excitation laser. The squared summation in equation (3) shall mimic the stochastic nature of the distribution of electron-ejection angles at the different spatial coordinates. The distance  $d$  of a (slow) electron-charge disk is assumed to grow proportionally with time  $t$  (neglecting collective space-charge effects within this charge sheet) described simply by

$$d(t) \simeq v_{\text{sheet}} t. \quad (4)$$

Fig. 2 shows numerical results of such calculations for three different longitudinal energies  $E_{\text{cloud}}^{\parallel}$  (corresponding to the  $z$ -velocity components  $v_{\text{sheet}}$ ) of the electrons that constitute the space-charge cloud. Using equations (3) and (4) in order to define the disk radius  $R$  in equation (2), we have solved

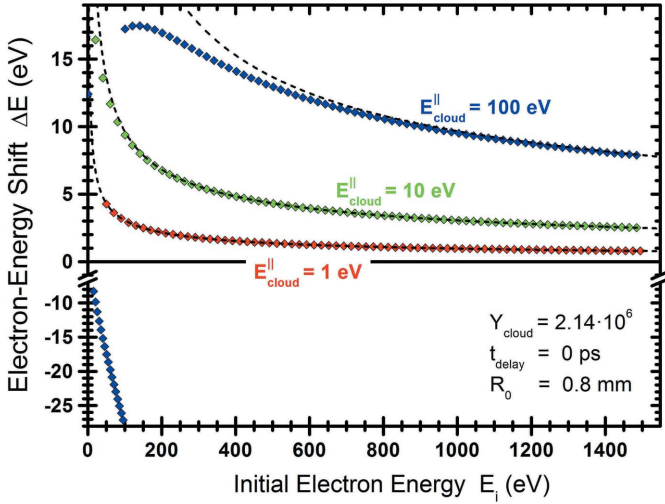


**Figure 2**  
Computed electron-energy shift  $\Delta E$  of test electrons interacting with a charge cloud at three different longitudinal energies (1 eV, 10 eV and 100 eV) as a function of the initial test-electron energy  $E_i$ . The dashed curves represent a fit, showing the scaling discussed in the text. Note the different axis styles above and below the y-axis break.

Newton's equation of motion for a test electron in the field of a dynamic charge cloud in front of a metal surface. Numerically, we have used a step-by-step integration using a modified Euler method with variable step length. A representative total number of ejected electrons per laser pulse  $Y_{\text{cloud}}$  was determined to be  $2.14 \times 10^6$  (from target-current measurements), for a mean laser power 150 mW, at a repetition frequency of 6.034 kHz. This value defines the charge  $Q$  and thus the constant  $c$  in equation (1). The choice of  $t_{\text{delay}} = 0$  means that the charge cloud and the test electron leave the surface at exactly the same point in time.

The numerical results are depicted by diamond symbols in the figure and show a deceleration ( $\Delta E < 0$ ) for test electron energies  $E_i$  below  $E_{\text{cloud}}^{\parallel}$  (see the blue symbols at energies below 100 eV). Contrary, for  $E_i > E_{\text{cloud}}^{\parallel}$  we find an acceleration of the test electron ( $\Delta E > 0$ ) that is monotonically diminishing with increasing test-electron energy. These results are consistent with the multi-particle simulations by Hellmann *et al.* (2009) (and references therein; see also Hellman *et al.*, 2012) and Zhou *et al.* (2005), who consider a self-consistent propagation of the electron cloud. In that work, however, the inelastic emission fractions and electron-cascade contributions were replaced by simple (more or less unknown) energy and angular distributions. Here we try to overcome this uncertainty by using information from our measured energy distributions.

In principle, one may compute a more realistic mean dynamic electric field  $E_z^{\text{dyn}}$  by integration of equation (2) over all electron energies with appropriate disk radii consistent with the double differential spectrum  $d^2Y_{\text{cloud}}/d\Omega dE'$  of the cloud electrons, considering the time distribution due to the excitation pulse and the electron transport in the bulk as well. From our point of view such a detailed calculation might be necessary if the electron–electron interaction is dominated by a single intense electron-energy peak, as was *ad hoc* assumed

in many previous investigations (Hellmann *et al.*, 2009; Zhou *et al.*, 2005). For our case, where the energies of space-charge electrons and test electrons are clearly separated, a much simpler approach is possible as will be explained in the following.

Calculations for different parameters sets and integration-step sizes indicate that the numerical uncertainties are far below 1%. Therefore, it was possible to extract an accurate scaling law from the results. The corresponding dashed curves for the energy shift  $\Delta E_{\text{scaling}}$  at high energies in Fig. 2 are given by

$$\Delta E_{\text{scaling}} = bY_{\text{cloud}}/R_0(E_{\text{cloud}}^{\parallel}/E_i)^{1/2}. \quad (5)$$

Note that the three curves contain only a single and common free parameter, namely  $b$  in equation (5). The parameter dependence in (5) is completely consistent with an approximate (Taylor) solution of the above equations for large times and small electric field strengths, where  $\Delta E$  is small compared with  $E_i$ . Also the value of  $b$  appears to be reasonable, as it is about twice as high as the result of an integral over the asymptotic solution. We find  $b = 1.14 \times 10^{-8}$  eV m (if  $\Delta E$  is measured in eV and  $R_0$  in m) from a fit to the highest test-electron energies  $E_i$ , for  $E_{\text{cloud}}^{\parallel} = 1$  eV. It is seen that the deviations exceed a few percent for  $E_i < 600$  eV at  $E_{\text{cloud}}^{\parallel} = 100$  eV. The linear behavior with respect to  $Y_{\text{cloud}}$  and the square-root relation between  $E_{\text{cloud}}$  and  $\Delta E$  suggest replacing the broad energy spectrum  $d^2Y_{\text{cloud}}/d\Omega dE'$  of the electron cloud by a single effective cloud energy  $E_{\text{cloud}}^{\text{eff}}$ , according to

$$E_{\text{cloud}}^{\text{eff}} = \left[ \int_0^{\infty} E'^{1/2} \frac{d^2Y_{\text{cloud}}}{d\Omega dE'} dE' / \int_0^{\infty} \frac{d^2Y_{\text{cloud}}}{d\Omega dE'} dE' \right]^2. \quad (6)$$

This replacement should yield accurate results, as long as  $E_{\text{cloud}} \ll E_i$ . Application of this formula to the rectangular energy distribution

$$\frac{d^2Y_{\text{cloud}}}{d\Omega dE'} = \begin{cases} c & \text{for } E_{\text{cloud}} < E_i \\ 0 & \text{otherwise} \end{cases}$$

of the cloud yields  $E_{\text{cloud}}^{\text{eff}} = (4/9)E_i$ . If inserted into (5), one may compare this specific result with the published energy shifts (Hellmann *et al.*, 2009) for this case (Figs. 2 and 7 of their 2009 paper). Note that very similar calculations (using also a simple constant angular distribution) have recently been performed with a time-optimized model by another group (Verna *et al.*, 2016). However, the neglect of image charges as well as alternatively static electronic holes in that model appears to be neither consistent with theory (Echenique *et al.*, 1979; Burgdörfer, 1987) nor with experimental data (Xiao *et al.*, 1997) on image-charge effects for fast charged particles. It turns out that we find nearly identical scaling properties, but our absolute energy shifts are about a factor of five higher than the previous results by Hellmann *et al.* Estimates for the fact that (i) we have used a point focus for the test electrons, whereas Hellmann *et al.* consider the test focus size to be equal to the cloud focus, and (ii) our calculations have been performed for a cosine angular distribution of the cloud

electrons whereas Hellmann *et al.* have used an isotropic distribution in Figs. 2 and 7 of their paper, indicate that also our absolute energy shift is in reasonable agreement with the previous theoretical data, since modifying the focal size and also the angular distribution [ $\alpha = 1$  rad in equation (3)] would reduce our calculated shifts by about a factor of two for each of the two effects. We take this agreement as a further confirmation of the high numerical accuracy of the above-defined approximate treatment.

As mentioned earlier we have left out a few (possibly minor) effects for the electron transport. The most problematic approximation might be the neglect of stochastic collisional perturbations, the so-called Boersch effect (Boersch, 1954; Jansen, 1988). For intermediate electron-scattering angles, collisions will lead to reduced energies of fast test electrons. However, for glancing angles and for head-on electron collisions the effect is zero. Furthermore, one must consider that electronic screening and Pauli blocking are important inside the solid as well as inside a dense electron cloud in front of the surface. Thus, one has to consider the differences inside and outside the solid in order to gain quantitative results, but this was not done in any of the model calculations known to us. We assume that the Boersch effect might have a considerable influence on line broadenings, but is not very important for the energy shift of fast test electrons.

#### 4. Results and discussion

In the following subsections, we present experimental electron-energy spectra and partial-yield (electron-yield) absorption-spectra. Fig. 3 displays a two-dimensional map of the electron count rate as an overview of the electron intensity as a function of the primary X-ray energy between 860 and

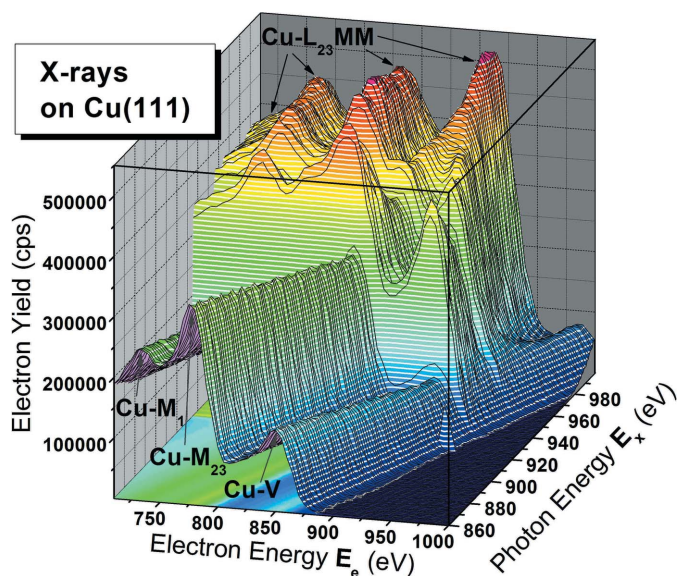


**Figure 3**  
Orthographic three-dimensional plot of the measured electron count rate versus emitted-electron energy and incident-photon energy (for horizontal X-ray polarization) in eV for a Cu(111) sample. Three different Cu photo-ionization peaks ( $M_1$ ,  $M_{23}$  and  $V$ , dominated by  $M_{45}$ ) and the Cu- $L_{23}MM$  Auger-electron group are marked in the plot.

1000 eV and the kinetic electron energy in the range 710–1000 eV. The peak structures are due to photoelectrons as well as Auger electrons liberated from a Cu(111) target by horizontally polarized X-rays (in-plane polarization in Fig. 1). The plot may be viewed as a case of near-edge X-ray absorption fine structure (NEXAFS) around the Cu- $L_3$  and  $-L_2$  edges, with resonance energies of 932.7 and 952.3 eV. Below these photon energies no Cu- $L$  vacancies are produced and the electron spectrum is solely due to photo-ionization of the Cu- $M$  shells (Courths & Hüfner, 1984; Powell & Mandl, 1972). The corresponding peaks are marked Cu- $M_1$ , Cu- $M_{23}$  and Cu- $V$  in the plot. The valence band peak (Cu- $V$ ) consists of a many-fold of states related to Cu- $M_{45}$ . These structures, however, cannot be separated with the electron-energy resolution of 3% as used in this work.

The Cu- $L_{23}MM$  Auger electron groups appear at photon energies above 932 eV where they are superimposed on the Cu- $M$  photoelectron peaks. Note that we have performed the experiments to be presented in the subsequent sections with vertical polarization of the X-ray beam (out-of-plane polarization in Fig. 1). For this case, the photo-ionization peaks are significantly reduced in comparison with the Cu- $LMM$  Auger structures. The Auger line structures as shown in Fig. 3 involve many different decay channels and have already been observed and interpreted in several previous investigations (Courths & Hüfner, 1984; Powell & Mandl, 1972; Roberts *et al.*, 1975; Kim *et al.*, 1976; Antonides *et al.*, 1977; Lund *et al.*, 1997; Föhlisch *et al.*, 2001). Our Auger electron spectra as well as the excitation curves as a function of the photon energy are consistent with the results of these previous investigations.

In principle, one may use such Auger-line structures and intensities, for example, to derive information about the degree of multiple ionization, about electronic screening, electron energy-loss and local electron temperature after ion excitation, with a time resolution of a few femtoseconds (given by the Auger decay rate; see Schiwietz *et al.*, 1999, 2010). In this work, we deal with a weak X-ray beam that leads nearly exclusively to single ionization at low electron temperatures, contrary to irradiation with fast heavy ions. The high-power IR laser beam, however, may increase the electron temperature and induce significant space-charge effects (Zhou *et al.*, 2005), as will be shown later. Before we discuss the corresponding pump-probe investigations, we will first concentrate on the continuous electron spectra induced by the laser beam alone.

##### 4.1. Hot-electron spectra

Fig. 4 displays three electron spectra induced by IR femtosecond laser pulses (the central laser wavelength is  $\lambda = 800$  nm with vertical laser polarization at the target spot and the pulse duration is about 100 fs) on Cu(111) and Cu(110) samples. Note that such polarization vectors in the target surface lead to a strong suppression of the electron emission (Luan *et al.*, 1989). The samples have been cleaned before the measurements and experiments have been performed at different grazing angles  $\Theta_g$ , laser repetition frequencies and laser powers (with peak power densities up to  $1.5 \times$

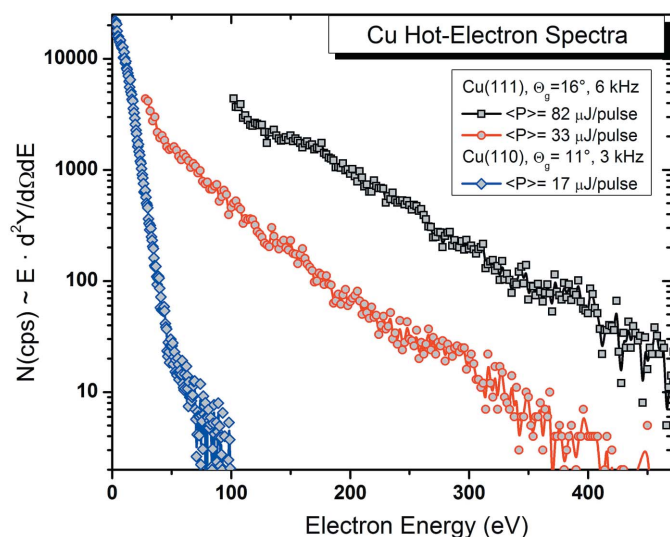


**Figure 4** Continuous spectra of (space-charge accelerated) electrons due to the interaction of a femtosecond-laser beam at  $\lambda = 800$  nm with Cu(110) and Cu(111) surfaces. Spectra have been taken at grazing angles of  $\Theta_g = 16^\circ$  and  $11^\circ$  with respect to the surface, at laser repetition frequencies of 6034 and 3017 Hz and at mean laser powers  $\langle P \rangle$  of 500 mW (82  $\mu\text{J}$  per pulse), 200 mW (33  $\mu\text{J}$  per pulse) and 50 mW (17  $\mu\text{J}$  per pulse).

$10^{11} \text{ W cm}^{-2}$ , corresponding to mean absorbed energies below about 0.3 eV atom $^{-1}$  pulse $^{-1}$ ). We have neither found a significant dependence of the spectra on  $\Theta_g$  (between  $11^\circ$  and  $16^\circ$ ) nor on the crystal face. However, we cannot exclude the influence of hot spots (related to surface roughness or surface-defect structures) on the spectra and on the total electron yields (Aeschlimann *et al.*, 1995; Nagel *et al.*, 2013). Furthermore, a detuning of the laser chirp (increased pulse width) results in steeper energy spectra. This influence on the electron spectra might be related to non-equilibrium effects in the electron system and fast energy relaxation of excited electrons (faster than the pulse length) or to intensity driven space-charge effects (Aeschlimann *et al.*, 1995).

The spectra are shown on a semi-logarithmic plot, because the electron yields are steeply decreasing as a function of energy. In principle, this may involve technical problems at low count rates as well as at high count rates. At low count rates ( $\ll 100$  counts  $\text{s}^{-1}$ ) dark noise in the microchannel-plate electron detector (Fraser *et al.*, 1987) and also in the detection electronics (cross-talk from external devices) may limit the statistical accuracy. By gating electron pulses with the laser trigger, we have reduced this noise by about three orders of magnitude. At very high count rates the measured intensities are limited by the laser repetition frequency ( $f_{\text{rep}} = 3$  kHz and 6 kHz for the present cases), since the detection electronics are not able to separate overlapping electron signals. The time-jitter inside the RBB spectrometer is just a few nanoseconds (Schiwietz *et al.*, 2015), and leads therefore to signal pile-up and count-rate saturation. Thus, for some cases we have additionally measured electron spectra at a significantly increased distance between target and spectrometer, where the electron count rate is reduced by an order of magnitude. The comparison of two such spectra enables a correction

function  $G$  for the true *versus* the detected count rate  $N_e$  {all spectra in Fig. 4 are corrected by the function  $G = [1.003 f_{\text{rep}}^4 / (1.003 f_{\text{rep}}^4 - N_e^4)]^{1/5}$ } to be extracted. Further, for the 50 mW spectrum in Fig. 4, we have combined two such spectra (after count-rate correction and intensity scaling), in order to reduce the statistical uncertainty at high electron energies (for low count rates) and to improve the accuracy at low electron energies (for count rates close to the laser repetition frequency).

For the characterization of the laser-induced dynamics (in Fig. 4 and for the rest of the paper) it would be interesting to know the mean number of electrons in excited states and/or the electron temperature in the focal spot. We have thus applied three different methods in order to estimate the electron temperatures for the cases considered in this work:

(I) A non-equilibrium electron temperature (Ferrini *et al.*, 2009; Fujimoto *et al.*, 1984) has been estimated from published IR absorption data [the corresponding reflectance values have been obtained from a data collection by Polyanskiy (2015)] neglecting ballistic and diffusive electronic heat transport as well as the heat coupling of the electronic degrees of freedom to the lattice. The neglect of ballistic heat transport into the bulk (Brorson *et al.*, 1987) and especially the increased absorption coefficient for a realistic (non-planar) surface in addition to the high excitation densities influence the corresponding uncertainties. Thus, we expect a range of electron temperatures increments between about 100 K and 3000 K for the different laser power densities used in this work, with uncertainties exceeding a factor of three [already the different experimental absorption values vary by about a factor four; see Polyanskiy (2015)].

(II) One may also analyze the shape of the measured electron spectra (Aeschlimann *et al.*, 1995; see also Schiwietz *et al.*, 1998, 1999) and try to relate the slope to an electron temperature by considering the differential electron flux of emitted hot electrons above the work function. This involves the electron density of states (eDOS) for valence and conduction bands, the Fermi–Dirac function, surface refraction (Rösler, 1995) and the experimental energy-resolution function (Schiwietz *et al.*, 2015). Electron temperatures extracted in this way from our measured spectra, however, appear to be unrealistically high, because detection of electrons below about 50 eV is significantly suppressed due to the influence of the earth’s magnetic field on the electron trajectories (consistent with the measured total target currents) and because space-charge acceleration [known from electron guns (Siwick *et al.*, 2002) and backscattered electrons (Cirelli *et al.*, 2009)] will boost the flux of high-energy electrons (Aeschlimann *et al.*, 1995; Petite *et al.*, 1992). As one may extract from Fig. 2, space-charge energy shifts and broadenings may exceed 10 eV at low energies, prohibiting any meaningful temperature analysis. Furthermore, a strong broadening of the cloud-electron spectra due to stochastic heating *via* individual electron–electron collisions is expected as well (Boersch, 1954; Jansen, 1988).

(III) Based on the Richardson–Dushman equation for electron emission at thermal equilibrium (Ready, 1965; Wang

*et al.*, 1994) (with a typical experimental current correction factor of  $\sim 0.3$ ) we compute electron temperatures between 3000 K and 4000 K from the number of emitted electrons per laser pulse (determined from the measured DC target current). These numbers are consistent with previous studies (Elsayed-Ali *et al.*, 1987), as well as with the rough estimate (I) and they are very insensitive to the accuracy of the focus diameter and the assumed duration of the heat pulse (we have used 100 fs for this value).

Thus, method (II) has to be disregarded and method (III) appears to yield the most realistic electron temperature results for the selected range of laser parameters. At very low laser powers, however, prompt multi-photon transitions (Aeschlimann *et al.*, 1995; Luan *et al.*, 1989) play a role and, at extremely high laser powers, MeV electrons are generated by ponderomotive forces due to electric field gradients (Oishi *et al.*, 2001) and these mechanisms are inconsistent with a temperature picture. Note furthermore that the resulting lattice-temperature rise is expected to be significantly lower than the electron temperature (because of cooling plus delayed coupling and the small ratio of electronic *versus* atomic heat capacities; see Schiwietz *et al.*, 2000). After some femtoseconds, there should be slight evaporation cooling of the hot electron gas close to the surface. After some further picoseconds in time, there is vibrational heat transport into the bulk of the Cu sample, leading to a strong temperature reduction (Kaganov *et al.*, 1956). Later there will be thermal equilibrium of the electron system and the atomic system (see, for example, Rethfeld *et al.*, 2002).

All spectra displayed in Fig. 4 are monotonically decreasing with energy. The spectra show a strong dependence on the laser peak power density. Electrons up to kinetic energies of a few hundred electronvolts are clearly visible (this is confirmed by the time-of-flight distributions that have been monitored with an oscilloscope). In principle, these high electron energies might correspond to extremely high multi-photon absorption probabilities, involving enormous excitation yields and high electron temperatures [see point (II) above]. As mentioned before, however, we expect a strong boost of fast electrons due to space-charge acceleration related to a huge amount of slower electrons that might even return towards the solid surface during the mutual repulsion with the faster electrons.

#### 4.2. Pump–probe NEXAFS

Fig. 5 displays two experimental NEXAFS spectra at the Cu- $L_3$  absorption edge (the step at about  $932.5 \pm 0.2$  eV). The  $L_{VV}$ -Auger electron count rate is measured by selecting the fixed kinetic electron energy of 910 eV, corresponding to the Cu- $L_3VV$  peak maximum, the right-most Auger peak in Fig. 3. We have used vertically polarized X-rays (out-of-plane polarization in Fig. 1) with nominal pulse widths of 16 to 24 ps FWHM (dependent on the bunch current in the so-called low- $\alpha$  mode B of BESSY II) at a grazing angle  $\Theta_g$  of  $22^\circ$  for this experiment. The energy axis is slightly rescaled by a constant factor, in order to fit the edge energy (half-width value) to the mean Cu- $L_3$  excitation energy, obtained from a weighted

average over five more accurate literature values (Lebugle *et al.*, 1981; Fuggle & Mårtensson, 1980).

The symbols (pink spheres) with statistical error bars show the fractional Cu- $L_{VV}$  count rate in coincidence with 6034 synchronized IR laser pulses per second (the mean laser power is 150 mW), the so-called gated yield. Thus, this gated yield is measured in the pump–probe mode with a fixed optimized timing between laser and so-called hybrid X-ray pulses (see next section). The time resolution of the RBB spectrometer ( $\Delta T = 2$  ns) is good enough to select only those electrons that stem from the laser-correlated bunch, since there are no other X-ray bunches in the vicinity of this hybrid bunch.

The (blue) solid line in Fig. 5 represents the non-coincident (total) Auger-electron count rate that is related to pure X-ray excitation. This total Auger yield is measured simultaneously to the gated yield and has been scaled down in intensity by more than four orders of magnitude to fit the other data set, consistent with the ratios of pulse frequencies and bunch currents. The natural line width of the Cu- $L_3$  vacancy is  $\sim 0.6$  eV (corresponding to a decay time of 1.1 fs) (Fuggle & Alvarado, 1980; Krause & Oliver, 1979) and the measured energy resolution is 2.5 eV (determined from a fit to the  $L_3$  edge). The structure of the spectra agrees roughly with total-electron-yield measurements for a polycrystalline Cu sample (Grioni *et al.*, 1989). However, the shape in Fig. 5 is in very good agreement with the results of Föhlisch *et al.* (2001), where the Auger-electron yield for Cu(110) was determined by peak integration of the Auger-electron peak for the dominant final state Cu- $L_3M_{4,5}M_{4,5}3d^8^1G_4$ .

In the previous section, we estimated an initial laser-induced rise of the electron temperature up to 4000 K. After

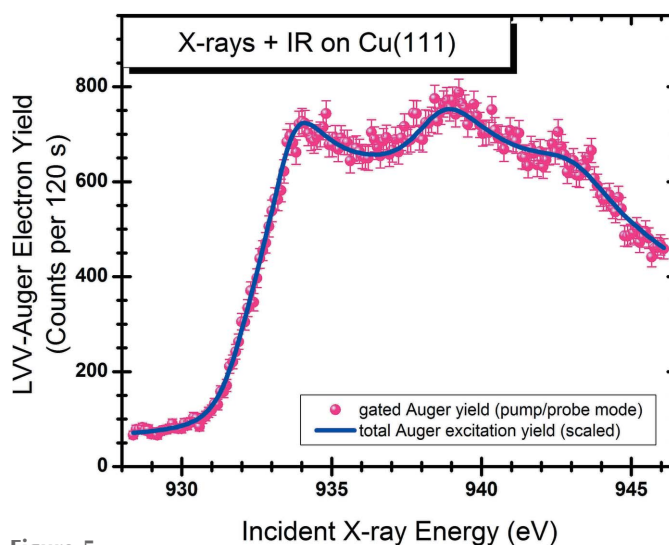


**Figure 5**  
NEXAFS spectrum given by the Cu- $L_{VV}$  Auger-electron peak intensity. The Cu- $L_3$  absorption edge is investigated in the pump–probe mode. The (blue) solid line represents the non-coincident (total) Auger-electron count rate that is related to pure X-ray excitation, scaled down by more than four orders of magnitude. The symbols with statistical error bars show the fractional Cu- $L_{VV}$  count rate in coincidence with 6034 synchronized IR laser pulses per second (the mean laser power is 150 mW), the so-called gated yield.

the energy transfer to the lattice, however, we expect neither a phase transition (the melting temperature of Cu is 1359 K) nor a strong influence of the electron-temperature rise on the electronic band structure (the Fermi temperature is  $1 \times 10^5$  K). From the comparison of both spectra (spheres and solid curve), it becomes clear that the IR laser irradiation has no visible effect on the Cu- $L_3VV$  Auger yield. A possible energy shift of the Cu- $L_3$  absorption edge would be below  $\pm 0.08$  eV, as has been determined from a fit. However, as our X-ray probe pulses average the detection over about 20 ps, there might still be a sizable laser effect existing on a sub-picosecond time scale.

### 4.3. Pump–probe electron spectra

Fig. 6 displays electron-energy spectra from a Cu(111) single crystal, measured at four different X-ray energies (namely  $E_x = 315, 515, 715$  and  $915$  eV). These spectra have been taken with vertically polarized X-rays (out-of-plane

polarization in Fig. 1) at a grazing angle  $\Theta_g$  of  $24^\circ$ . Since the X-ray energies are below the  $L$  ionization thresholds (see Fig. 3 for comparison), all structures in the spectra are due to photo-ionization of valence electrons (the  $M_{45}$  states plus the de-localized  $N_1$  band) and the somewhat more strongly bound shells (marked  $M_{23}$  and  $M_1$ ). Before we turn to the dynamics induced by laser excitation, we first discuss the spectral structures (peak positions and intensities).

It may be seen from the figure that the photoelectron peaks show a relatively sharp drop-off at high electron energies and a much more flat low-energy slope. The sharp drop-off is consistent with the relative energy-resolution of  $\Delta E/E = 3\%$  of the actual version of the RBB (Schiwietz *et al.*, 2015). Thus, we cannot resolve spin-orbit splitting and the electronic valence-band structure at such high electron energies. The continuous electron intensity below the maxima of all photoelectron peaks is due to electrons that have suffered a few inelastic energy losses. These energy losses are related to various basic electron-transport processes, *e.g.* surface- and bulk-plasmon production as well as intra- and inter-band excitations. The peak maxima agree very well with published binding energies for Cu (Fuggle & Mårtensson, 1980; Lebugle *et al.*, 1981) when the finite resolution is accounted for.

Considering electron mean-free-paths and spectrometer resolution, we extract a ratio of differential photoelectron cross sections  $dCS(M_1):dCS(M_{23}):dCS(V) = 0.16:1:1.18$  from our experimental spectrum taken for  $E_x = 515$  eV. Together with the angle-dependent squared differential dipole matrix elements the population numbers (2:6:11 electrons) determine the peak intensities in first-order perturbation theory (McGuire, 1968; Scofield, 1976; Manson & Cooper, 1968). A standard theory tabulation (Yeh & Lindau, 1985) yields 0.26:1:0.77 for Cu atoms. The deviations of about 50% from the experimental results reflect that neither solid-state wavefunctions have been used in the tabulation, nor was the  $l$ -dependent angular distribution of photoelectrons accounted for. Thus, the gross structures of the Cu spectra in Fig. 6 are relatively well understood on the basis of a simple central-field model and we may focus on the dynamical effects triggered by laser excitation.

Each of the four plots in Fig. 6 contains three different spectra (a thin and a thick solid curve, and solid symbols). The solid diamonds have been taken in the pump–probe mode for a fixed mean laser power of 150 mW at a laser repetition frequency of 6 kHz (for similar parameters as the gated yield in Fig. 5). For these data sets there is ionization by the X-ray beam with synchronized laser pulses of 100 fs width at the same target spot. The optimum time difference between laser pulse and X-ray pulse at the target is close to zero, as determined from the corresponding APD signals with an uncertainty of about  $\pm 25$  ps (details of the corresponding experimental and theoretical delay-time distributions will be published in a forthcoming paper). Each of these data points contains about 100 counts in the valence-band peak, which explains the statistical scatter of the results of about 10%.

The thin red lines are reference data, showing spectra that correspond to X-ray ionization without simultaneous femto-

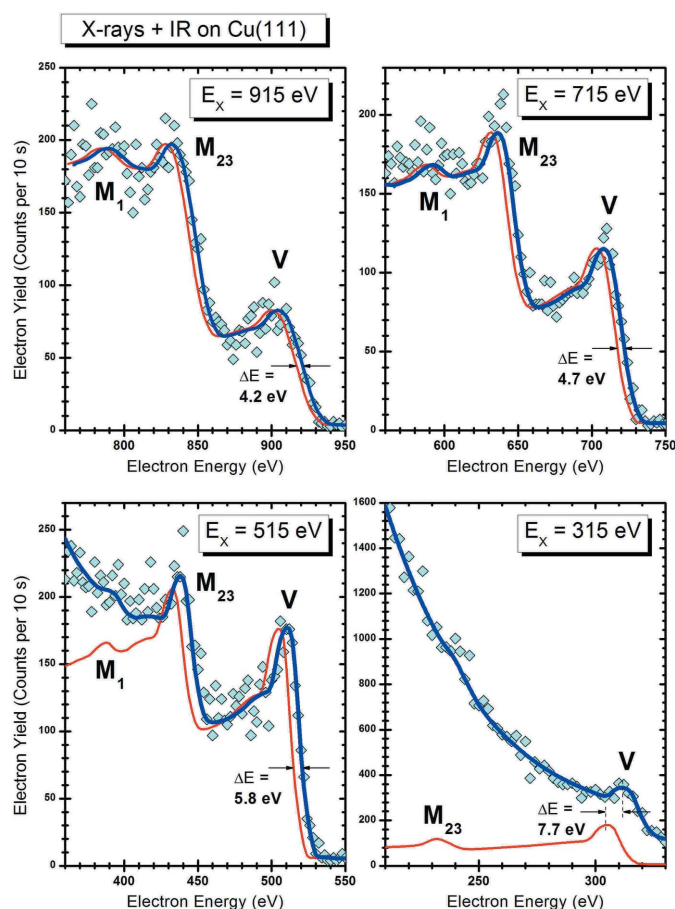


**Figure 6** Electron-energy spectra for photo-emitted Cu(111) valence electrons (rightmost peaks, Cu- $V$ ) as well as Cu- $M_{23}$  and Cu- $M_1$ . The solid symbols have been measured in the pump–probe mode and the thin red lines are experimental reference data without laser excitation (the thick solid blue fit curves are explained in the text). Four cases for different incident photon energies  $E_x$  (315, 515, 715 and 915 eV) are displayed in separate plots. The mean laser power is 150 mW in all cases and data have been taken for vertically polarized X-rays at a grazing angle  $\Theta_g$  of  $24^\circ$ .

second-laser excitation. These spectra result from the total (ungated) electron count rate in the spectrometer, without any timing requirement, and the laser-shot frequency is too low to have any significant influence on these data. For these thin red curves, the total electron counts have been scaled down in intensity by more than four orders of magnitude to fit the pump–probe valence-band intensity. Note that the corresponding normalization factors are described within a few percent by the given laser-repetition frequency and the hybrid-bunch currents relative to the total storage-ring currents.

The thick (blue) solid curves in Fig. 6 are identical to the thin ones, except for two modifications. We have applied a constant energy shift (see the arrows and the energy offsets  $\Delta E$  in the plots) and added an intensity contribution due to hot electrons (an exponential function, similar to Fig. 4). The latter contribution is only significant for the two spectra with the lowest photon and electron energies. Specifically for the photon energy of 315 eV, a stable fit of the energy shift is strongly dependent on an accurate iteration of the hot-electron contribution. Note that the energy shifts in the solid curves have been adjusted to the high-energy slopes of the pump–probe valence-band peak in each of the spectra. Thus, the solid curves agree very well with the pump–probe data at the higher electron energies.

The results show a clear energy gain for the laser excited case (thick solid curves and colored symbols) compared with photo-ionization from the non-excited surface (thin red curves). For the given cases in Fig. 6, the Cu- $V$  peaks are shifted towards higher energy by 4.2 to 7.7 eV dependent on the emitted electron energy. Before we discuss details of the spectra in Fig. 6 and turn to a quantitative discussion, we first want to show that the measured energy gains are clearly related to space-charge accelerations. In principle, a variety of different effects can lead to an energy shift of ejected particles:

(i) Especially in insulators, high ionization yields may lead to positive (microscopic) surface charges that decelerate emitted electrons. Such decelerations of convoy electrons (Xiao *et al.*, 1997) and Auger electrons (Schiwietz *et al.*, 1992) have been observed in ion-solid interactions.

(ii) Electrons (Xiao *et al.*, 1997) or ions (Kurz *et al.*, 1994) themselves experience an image-charge acceleration in front of a surface. However, this is already part of the electronic surface work-function and might only slightly be modified by laser excitation (through a change of the electronic polarizability).

(iii) Intense ultrashort laser pulses may lead to electron acceleration by wake-field forces inside dense matter (Malka *et al.*, 2002).

(iv) Binding energies and correspondingly photoelectron energies and Auger energies may be influenced by the laser excitation, *via* a modification of the electronic screening or the electronic density-of-states. Also virtual excitations and the corresponding AC Stark shift may become important.

(v) The high density of laser-induced slow electrons in front of a surface may speed-up faster electrons as a result of the mutual electron repulsion (space-charge acceleration).

We may exclude point (i), because the target is neither an insulator nor do we observe a deceleration. The total work function of Cu is 4.6 eV and, thus, the observed shifts are much too high to be explained by point (ii). The laser power densities in this work are orders-of-magnitude too low to yield significant wake-field forces inside the solid [see point (iii)]. When averaged over the pulse width, the strongly localized  $L_3$ -shell electrons do have constant binding energies, not dependent on the laser excitation (see §4.2 and Fig. 5). Thus, point (iv) may be excluded, since we do not observe inconsistent energy shifts for the partly de-localized valence states ( $V$ ) and the localized bound states ( $M_{23}$ ). Hence, we come to the conclusion that space-charge acceleration near to the Cu surface [point (v)] is responsible for the observed energy shifts. Space-charge effects at surfaces, such as electron suppression (Fujimoto *et al.*, 1984) and electron accelerations (Dell'Angela *et al.*, 2015; Gilton *et al.*, 1990; Passlack *et al.*, 2006; Pietzsch *et al.*, 2008; Qian & Elsayed-Ali, 2003; Zhou *et al.*, 2005), have also been reported by other authors and for laser pump-pulses they are related to the spectral yield of laser induced electrons (see §2 and §4.1).

Comparing the thick solid curve (rescaled reference data) and the diamond symbols (pump–probe results) in more detail, there are indications for two small remaining deviations. First, a statistical analysis of the ratio of  $M_{23}$  to valence-band peak intensities shows that there is an intensity enhancement by  $4.5 \pm 1.7\%$  (for the four spectra with clear  $M_{23}$  photoionization peaks) in the pump–probe yield. This small effect might be related to a remaining valence-band modification by the laser. Second, we find slightly different energy shifts for the structures below the valence-band peak, as discussed in the residual part of this section.

Fig. 7 displays energy shifts evaluated from the deviations of pump–probe and reference electron spectra at the photo-ionization peaks (Cu- $V$  as well as Cu- $M_{23}$ ) below the Cu- $L_3$  threshold. In addition, above the Cu- $L_3$  threshold, up to three Auger peaks (Cu- $L_3M_{2,3}M_{2,3}$ , Cu- $L_3M_{2,3}V$ , Cu- $L_3VV$  as in Fig. 2) have been evaluated as well. The closed (colored) symbols in Fig. 7 have been determined from photo-ionization peaks at different X-ray energies. Contrary, all open symbols are related to shifts of Auger-electron peaks. The data in Fig. 7 are presented as a function of the electron-peak energy, since a pre-analysis of all the spectra has revealed no extra dependence on the primary photon energy. The evaluation uses the same type of fit as described for the valence band in connection with Fig. 6. For Auger-electron spectra taken with good statistics, the peak maxima were used directly to determine the energy shifts. For all other spectra, it turned out that the accuracy of the evaluation may be increased by using the half-height of the high-energy slopes of the peaks (the corresponding electron peak position was then corrected for the experimental energy resolution).

The different symbol types in Fig. 7 represent different mean IR laser powers, ranging from 75 to 200 mW at fixed laser repetition frequency of 6 kHz. For fixed laser power it is seen that the shifts are monotonically decreasing with increasing kinetic electron energy. Neither the primary photon

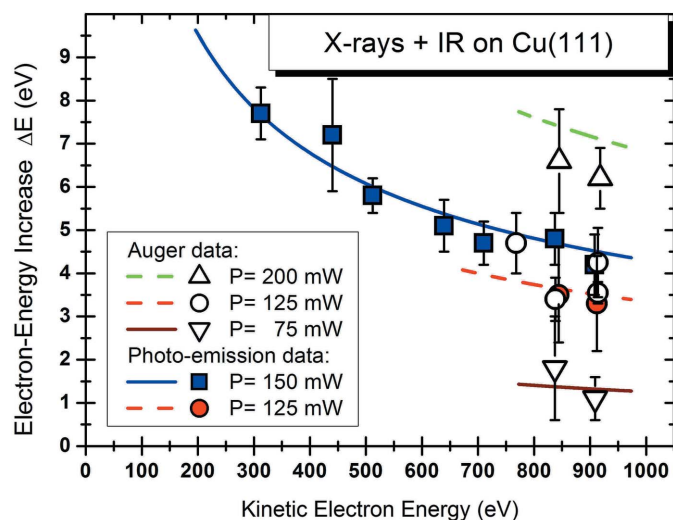


**Figure 7** Electron-energy enhancements extracted from the energy difference of electron peaks with and without the IR pump-laser beam. Results have been obtained for different photon energies and IR laser powers: at mean values of 200 mW (open up triangles), 150 mW (blue squares), 125 mW (red and open circles) and 75 mW (open down triangle). Closed (colored) symbols indicate values that have been determined from photo-ionization peaks. All open symbols are related to shifts of Auger-electron peaks and the curves correspond to the absolute theoretical results (multiplied by a common factor of 1.22) for the four different laser powers as described in the text.

energy (between 315 and 931 eV) nor the electron production mechanism (Auger or photoelectron) seem to have any influence on the results. As the decay time of the Cu- $L_3$  vacancy is about 1.1 fs (Fuggle & Alvarado, 1980; Krause & Oliver, 1979), both reaction channels (photo-ionization and Auger decay) are prompt in comparison with the X-ray pulse-width and even to the laser pulse-width, suggesting that the electron transport is only affected by the IR laser and not by the primary excitation/ionization process. The results for 837 to 918 eV clearly indicate that the electron-energy increase is higher at higher laser-power densities.

The colored solid and dashed lines correspond to full *ab initio* calculations using equations (1)–(4), as used also for the symbols in Fig. 2. The effective cloud energies  $E_{\text{cloud}}^{\text{eff}}$  for these computations have been estimated from measured hot-electron energy distributions (as in Fig. 4) according to equation (6). The interpolated results for this parameter are 6.1, 9.3, 10.0 and 12.0 eV for laser powers of 75, 125, 150 and 200 mW at a 6 kHz repetition rate. These four theoretical curves have been multiplied by a common factor of 1.22 in order to fit the experimental energy shifts. It is seen that the shape of these functions agrees very well with the experimental data. Only the 200 mW results are slightly overestimated by the scaled model results. For this case, the cloud-electron density might be so high that there is a redistribution of electrons within the cloud (Coulomb explosion), turning the corresponding angular distribution from cosine into isotropic (such an effect is consistent with the results of Fig. 2). The all-over correction factor of 1.22 would relate to an overestimated focal size of the laser spot by a factor of 1.22 or by an uncertainty of the effective cloud energies by a factor of 1.5. A

mixture of both uncertainties might be responsible for the remaining deviations between theory and experiment. However, one also has to consider that the experiment has been performed under grazing conditions with an elliptical laser spot on the target, whereas the current model assumes a circular spot (with the geometrical mean radius, keeping the correct area electron-density).

## 5. Conclusions and outlook

We have investigated the properties of ejected electrons (between about 10 and 1000 eV) from atomically clean crystalline Cu samples as a result of X-ray photo-ionization (photon energies between about 300 and 1000 eV) and Auger decay, both influenced by strong laser excitation (time-resolved XPS and Auger emission). The laser-power densities in these laser-pump X-ray-probe experiments range from  $3 \times 10^{10}$  to  $1.5 \times 10^{11} \text{ W cm}^{-2}$ , just slightly below the material-damage threshold. Our newly developed electrostatic electron spectrometer (the retarding Bessel box RBB) has been used for this purpose. Measurements of IR-laser-induced electrons show a significant intensity of fast electrons at high laser powers, extending beyond kinetic energies of 400 eV. As this flat electron emission spectrum is completely inconsistent (neglecting electron–electron interactions in the continuum) with the estimated electron temperatures, space-charge effects are the most likely explanations of such broad spectra due to high-power laser–solid interactions. This includes stochastic collision processes due to the residual electron–electron interaction in the continuum, as well as mean-field space-charge acceleration (and deceleration). The latter is consistent with our theoretical estimates for the energy shifts.

We do not find a significant laser-pump effect in the NEXAFS spectra. In principle, core-hole energies and absorption edges should be shifted and near-edge structures might also be slightly modified for electron temperatures between 3000 K and 4000 K. The current time resolution of about 30 ps might be the reason why none of these effects have been found.

Using the same experimental settings, however, a clear acceleration of Auger and also photoelectrons by up to 7.7 eV has been detected for various primary X-ray energies and laser powers in the pump–probe measurements. Thus, the measured variation of photoelectron as well as Auger-electron energies is not related to a laser-induced core-hole energy shift. Delay-time scans indicate that the detected electron-energy shifts are related to an effect on the picosecond time scale. This is consistent with results and guesses within previous time-resolved photoelectron spectroscopy experiments by other groups (Dell’Angela *et al.*, 2015; Gilton *et al.*, 1990; Passlack *et al.*, 2006; Pietzsch *et al.*, 2008; Qian & Elsayed-Ali, 2003; Zhou *et al.*, 2005). Note that we have performed the most comprehensive of such investigations, covering a variation of the time delay, of the X-ray energy, of the emission process and of the laser power, including a characterization of the low-energy electron spectra and total

electron yields that determine the shift of the high-energy peaks.

In fact, it turns out that there is no difference visible between the shifts observed for the two electron-emission mechanisms (Auger decay and photoelectron production) and there are monotonous dependencies on the laser power and on the ejected-electron energy. This is consistent with previous simulations of vacuum space-charge effects (Dell'Angela *et al.*, 2015; Gilton *et al.*, 1990; Hellmann *et al.*, 2009; Passlack *et al.*, 2006; Pietzsch *et al.*, 2008; Qian & Elsayed-Ali, 2003; Verna *et al.*, 2016; Zhou *et al.*, 2005). Furthermore, the measured energy and power dependencies agree perfectly with our *ab initio* space-charge calculations, when a fixed small correction factor is accounted for.

In summary, we have not only performed our experiments with a well defined metallic target but we have also characterized the boundary conditions of space-charge acceleration by determining the corresponding trigger mechanism, thereby excluding other possible reasons for electron energy shifts. We have found extremely strong vacuum space-charge effects for the laser-induced emitted electron cloud and also clear effects for X-ray driven electron emission during laser irradiation. Both results are in accord with our *ab initio* calculations, indicating a predictive power of the model and a possible future application of the XPS method also at free-electron lasers.

## Acknowledgements

We are indebted to the BESSY II synchrotron crew, to R. Mitzner for his help at the pump laser and to M. Beye as well as A. Pietzsch for helpful comments. We also thank M. Beye for his contributions during the initial preparation phase of this experiment. It is noted that the setup was mainly financed *via* the Helmholtz strategy fund 'Ionenspuren in Festkörpern' (2000–2005). Last, but not least, we should mention the help of the BESSY mechanics workshop and of T. Blume regarding the stepwise optimization of the RBB spectrometer and our ET chamber.

## References

- Aeschlimann, M., Schmuttenmaer, C. A., Elsayed-Ali, H. E., Miller, R. J. D., Cao, J., Gao, Y. & Mantell, D. A. (1995). *J. Chem. Phys.* **102**, 8606–8613.
- Antonides, E., Janse, E. C. & Sawatzky, G. A. (1977). *Phys. Rev. B*, **15**, 1669–1679.
- Arista, N. R. & Brandt, W. (1984). *Phys. Rev. A*, **29**, 1471–1480.
- Baggesen, J. C. & Madsen, L. B. (2008). *Phys. Rev. A*, **78**, 032903.
- Bergara, A., Pitarke, J. M. & García de Abajo, F. J. (1998). *Nucl. Instrum. Methods Phys. Res. B*, **135**, 97–102.
- Boersch, H. (1954). *Z. Phys.* **139**, 115–146.
- Borisov, A., Sánchez-Portal, D., Díez Muñoz, R. & Echenique, P. M. (2004). *Chem. Phys. Lett.* **387**, 95–100.
- Brorson, S. D., Fujimoto, J. G. & Ippen, E. P. (1987). *Phys. Rev. Lett.* **59**, 1962–1965.
- Burgdörfer, J. (1987). *Nucl. Instrum. Methods Phys. Res. B*, **24–25**, 139–142.
- Campillo, I., Pitarke, J. M., Rubio, A., Zarate, E. & Echenique, P. M. (1999). *Phys. Rev. Lett.* **83**, 2230–2233.
- Cao, J., Gao, Y., Miller, R. J. D., Elsayed-Ali, H. E. & Mantell, D. A. (1997). *Phys. Rev. B*, **56**, 1099–1102.
- Cirelli, C., Hengsberger, M., Dolocan, A., Over, H., Osterwalder, J. & Greber, T. (2009). *Europhys. Lett.* **85**, 17010.
- Courths, R. & Hüfner, S. (1984). *Phys. Rep.* **112**, 53–171.
- Dell'Angela, M., Anniyev, T., Beye, M., Coffee, R., Föhlisch, A., Gladh, J., Kaya, S., Katayama, T., Krupin, O., Nilsson, A., Nordlund, D., Schlotter, W. F., Sellberg, J. A., Sorgenfrei, F., Turner, J. J., Öström, H., Ogasawara, H., Wolf, M. & Wurth, W. (2015). *Struct. Dynam.* **2**, 025101.
- Echenique, P. M. (2007). Private communication.
- Echenique, P. M., Ritchie, R. H. & Brandt, W. (1979). *Phys. Rev. B*, **20**, 2567–2580.
- Elsayed-Ali, H. E., Norris, T. B., Pessot, M. A. & Mourou, G. A. (1987). *Phys. Rev. Lett.* **58**, 1212–1215.
- Fann, W. S., Storz, R., Tom, H. W. K. & Bokor, J. (1992). *Phys. Rev. B*, **46**, 13592–13595.
- Ferrini, G., Banfi, F., Giannetti, C. & Parmigiani, F. (2009). *Nucl. Instrum. Methods Phys. Res. A*, **601**, 123–131.
- Föhlisch, A., Karis, O., Weinelt, M., Hasselström, J., Nilsson, A. & Mårtensson, N. (2001). *Phys. Rev. Lett.* **88**, 027601.
- Fraser, G. W., Pearson, J. F. & Lees, J. E. (1987). *Nucl. Instrum. Methods Phys. Res. A*, **254**, 447–462.
- Fuggle, J. C. & Alvarado, S. F. (1980). *Phys. Rev. A*, **22**, 1615–1624.
- Fuggle, J. C. & Mårtensson, N. (1980). *J. Electron Spectrosc. Relat. Phenom.* **21**, 275–281.
- Fujimoto, J. G., Liu, J. M., Ippen, E. P. & Bloembergen, N. (1984). *Phys. Rev. Lett.* **53**, 1837–1840.
- Gilton, T. L., Cowin, J. P., Kubiak, G. D. & Hamza, A. V. (1990). *J. Appl. Phys.* **68**, 4802.
- Gregoratti, L., Mentis, T. O., Locatelli, A. & Kiskinova, M. (2009). *J. Electron Spectrosc. Relat. Phenom.* **170**, 13–18.
- Griioni, M., Goedkoop, J. B., Schoorl, R., de Groot, F. M. F., Fuggle, J. C., Schäfers, F., Koch, E. E., Rossi, G., Esteva, J.-M. & Karnatak, R. C. (1989). *Phys. Rev. B*, **39**, 1541–1545.
- Hellmann, S., Rossnagel, K., Marczyński-Bühlow, M. & Kipp, L. (2009). *Phys. Rev. B*, **79**, 035402.
- Hellmann, S., Sohrt, C., Beye, M., Rohwer, T., Sorgenfrei, F., Marczyński-Bühlow, M., Kalläne, M., Redlin, H., Hennies, F., Bauer, M., Föhlisch, A., Kipp, L., Wurth W. & Rossnagel, K. (2012). *New J. Phys.* **14**, 013062.
- Henke, B. L., Gullikson, E. M. & Davis, J. C. (1993). *At. Data Nucl. Data Tables*, **54**, 181–342.
- Hollmack, K., Bahrtdt, J., Balzer, A., Bovensiepen, U., Brzhezinskaya, M., Erko, A., Eschenlohr, A., Follath, R., Firsov, A., Frentrup, W., Le Guyader, L., Kachel, T., Kuske, P., Mitzner, R., Müller, R., Pontius, N., Quast, T., Radu, I., Schmidt, J.-S., Schüßler-Langeheine, C., Sperling, M., Stamm, C., Trabant, C. & Föhlisch, A. (2014). *J. Synchrotron Rad.* **21**, 1090–1104.
- Jansen, G. H. (1988). *J. Vac. Sci. Technol. B*, **6**, 1977–1983.
- Kachel, T. (2016). *J. Large-Scale Res. Facil.* **2**, A48.
- Kaganov, M. O., Lifshits, I. M. & Tanatarov, L. V. (1956). *Zh. Eksp. Teor. Fiz.* **31**, 232. [(1957). *Sov. Phys. JETP*, **4**, 173; *ibid* (1959). *At. Energy*, **6**, 391.]
- Kim, K. S., Gaarenstroom, S. W. & Winograd, N. (1976). *Chem. Phys. Lett.* **41**, 503–506.
- Knoesel, E., Hotzel, A. & Wolf, M. (1998). *Phys. Rev. B*, **57**, 12812–12824.
- Krause, M. & Oliver, J. H. (1979). *J. Phys. Chem. Ref. Data*, **8**, 329.
- Kurz, H., Aumayr, F., Winter, H. P., Schneider, D., Briere, M. A. & McDonald, J. W. (1994). *Phys. Rev. A*, **49**, 4693–4702.
- Lebugle, A., Axelsson, U., Nyholm, R. & Mårtensson, N. (1981). *Phys. Scr.* **23**, 825–827.
- Lemell, C., Tong, X.-M., Krausz, F. & Burgdörfer, J. (2003). *Phys. Rev. Lett.* **90**, 076403.
- Lisowski, M., Loukakos, P. A., Bovensiepen, U. & Wolf, M. (2004). *Appl. Phys. A*, **79**, 739–741.

- Luan, S., Hippler, R., Schwier, H. & Lutz, H. (1989). *Europhys. Lett.* **9**, 489–494.
- Lund, C. P., Thurgate, S. M. & Wedding, A. B. (1997). *Phys. Rev. B*, **55**, 5455–5465.
- Malka, V., Fritzler, S., Lefebvre, E., Aleonard, M.-M., Burgy, F., Chambaret, J.-P., Chemin, J.-F., Krushelnick, K., Malka, G., Mangels, S. P. D., Najmudin, Z., Pittman, M., Rousseau, J.-P., Scheurer, J.-N., Walton, B. & Dangor, A. E. (2002). *Science*, **298**, 1596–1600.
- Manson, S. T. & Cooper, J. W. (1968). *Phys. Rev.* **165**, 126–138.
- Martynenko, Yu. V. & Yavlinskii, Yu. N. (1983). *Sov. Phys. Dokl.* **28**, 391–392.
- McGuire, E. J. (1968). *Phys. Rev.* **175**, 20–30.
- Nagel, P. M., Robinson, J. S., Harteneck, B. D., Pfeifer, T., Abel, M. J., Prell, J. S., Neumark, D. M., Kaindl, R. A. & Leone, S. R. (2013). *Chem. Phys.* **414**, 106–111.
- NIST (2000). *Standard Reference Database 71, NIST Electron Inelastic Mean-Free-Path Database*, Version 1.1; edited by C. J. Powell and A. Jablonski. NIST, Gaithersburg, MD, USA.
- NIST (2005). *Standard Reference Database 100 for the Simulation of Electron Spectra for Surface Analysis (SESSA 1.1)*. NIST, Gaithersburg, MD, USA.
- Ogawa, S., Nagano, H. & Petek, H. (1997). *Phys. Rev. B*, **55**, 10869–10877.
- Oishi, Y., Nayuki, T., Nemoto, K., Okano, Y., Hironaka, Y., Nakamura, K. G. & Kondo, K. (2001). *Appl. Phys. Lett.* **79**, 1234–1236.
- Passlack, S., Mathias, S., Andreyev, O., Mittnacht, D., Aeschlimann, M. & Bauer, M. (2006). *J. Appl. Phys.* **100**, 024912.
- Petek, H., Nagano, H. & Ogawa, S. (1999). *Phys. Rev. Lett.* **83**, 832–835.
- Petite, G., Agostini, P., Trainham, R., Mevel, E. & Martin, Ph. (1992). *Phys. Rev. B*, **45**, 12210–12217.
- Pietzsch, A., Föhlich, A., Beye, M., Deppe, M., Hennies, F., Nagasono, M., Suljoti, E., Wurth, W., Gahl, C., Döbrich, K. & Melnikov, A. (2008). *New J. Phys.* **10**, 033004.
- Polyanskiy, M. N. (2015). *Refractive index database*, <http://refractiveindex.info> (accessed February 2015)
- Pontius, N., Holldack, K., Schüßler-Langeheine, C., Kachel, T. & Mitzner, R. (2016). *J. Large-Scale Res. Facil.* **2**, A46.
- Powell, C. J. & Mandl, A. (1972). *Phys. Rev. B*, **6**, 4418–4429.
- Qian, B.-L. & Elsayed-Ali, H. E. (2003). *J. Appl. Phys.* **94**, 803.
- Ready, J. F. (1965). *Phys. Rev.* **137**, A620–A623.
- Rethfeld, B., Kaiser, A., Vicanek, M. & Simon, G. (2002). *Phys. Rev. B*, **65**, 214303.
- Roberts, E. D., Weightman, P. & Johnson, C. E. (1975). *J. Phys. C*, **8**, L301–L304.
- Rösler, M. (1995). *Appl. Phys. A*, **61**, 595–607.
- Schiwietz, G., Beye, M., Kühn, D. & Xiao, G. (2015). *J. Electron Spectrosc. Relat. Phenom.* **203**, 51–59.
- Schiwietz, G., Czerski, K., Hellhammer, R., Roth, M., Staufenbiel, F., Fadanelli, R. C. & Grande, P. L. (2008). *Nucl. Instrum. Methods Phys. Res. B*, **266**, 1287–1293.
- Schiwietz, G., Czerski, K., Roth, M., Grande, P. L., Koteski, V. & Staufenbiel, F. (2010). *Phys. Rev. Lett.* **105**, 187603.
- Schiwietz, G., Czerski, K., Roth, M., Staufenbiel, F. & Grande, P. L. (2004). *Nucl. Instrum. Methods Phys. Res. B*, **226**, 683–704.
- Schiwietz, G., Grande, P. L., Skogvall, B., Biersack, J. P., Köhrbrück, R., Sommer, K., Schmoltdt, A., Goppelt, P., Kádár, I., Ricz, S. & Stettner, U. (1992). *Phys. Rev. Lett.* **69**, 628–631.
- Schiwietz, G., Roth, M., Czerski, K., Staufenbiel, F. & Grande, P. L. (2007). *Phys. Rev. Lett.* **99**, 197602.
- Schiwietz, G., Xiao, G., Grande, P. L., Luderer, E., Pazirandeh, R. & Stettner, U. (1998). *Nucl. Instrum. Methods Phys. Res. B*, **146**, 131–136.
- Schiwietz, G., Xiao, G., Grande, P. L., Luderer, E., Pazirandeh, R. & Stettner, U. (1999). *Europhys. Lett.* **47**, 384–390.
- Schiwietz, G., Xiao, G., Luderer, E. & Grande, P. L. (2000). *Nucl. Instrum. Methods Phys. Res. B*, **164–165**, 353–364.
- Schmittenmaer, C. A., Aeschlimann, M., Elsayed-Ali, H. E., Miller, R. J. D., Mantell, D. A., Cao, J. & Gao, Y. (1994). *Phys. Rev. B*, **50**, 8957–8960.
- Schönhense, G., Medjanik, K., Tusche, C., de Loos, M., van der Geer, B., Scholz, M., Hieke, F., Gerken, N., Kirschner, J. & Wurth, W. (2015). *Ultramicroscopy*, **159**, 488–496.
- Scofield, J. H. (1976). *J. Electron Spectrosc. Relat. Phenom.* **8**, 129–137.
- Silvestrelli, P. L., Alavi, A., Parrinello, M. & Frenkel, D. (1996). *Phys. Rev. Lett.* **77**, 3149–3152.
- Siwick, B. J., Dwyer, J. R., Jordan, R. E. & Miller, R. J. D. (2002). *J. Appl. Phys.* **92**, 1643–1648.
- Smekal, W., Werner, W. S. M. & Powell, C. J. (2005). *Surf. Interface Anal.* **37**, 1059–1067.
- Stampfli, P. & Bennemann, K. H. (1994). *Phys. Rev. B*, **49**, 7299–7305.
- Verna, A., Greco, G., Lollobrigida, V., Offi, F. & Stefani, G. (2016). *J. Electron Spectrosc. Relat. Phenom.* **209**, 14–25.
- Wall, S., Foglia, L., Wegkamp, D., Appavoo, K., Nag, J., Haglund, R. F., Stähler, J. & Wolf, M. (2013). *Phys. Rev. B*, **87**, 115126.
- Wang, X. Y., Riffe, D. M., Lee, Y.-S. & Downer, M. C. (1994). *Phys. Rev. B*, **50**, 8016–8019.
- Xiao, G., Schiwietz, G., Grande, P. L., Stolterfoht, N., Schmoltdt, A., Grether, M., Köhrbrück, R., Spieler, A. & Stettner, U. (1997). *Phys. Rev. Lett.* **79**, 1821–1824.
- Yeh, J.-J. & Lindau, I. (1985). *At. Data Nucl. Data Tables*, **32**, 1–155.
- Zhou, X. J., Wannberg, B., Yang, W. L., Brouet, V., Sun, Z., Douglas, J. F., Dessau, D., Hussain, Z. & Shen, Z.-X. (2005). *J. Electron Spectrosc. Relat. Phenom.* **142**, 27–38.